RESEARCH ARTICLE
ATMOSPHERIC PHYSICS

Earth and Planetary Physics
7: 655–664, 2023
doi: 10.26464/epp2023081

Middle and near ultraviolet spectrograph of the Scientific Experimental system in Near SpacE (SENSE)

Xin Sun[1,2*], DaLian Shi[1,2], Zhen Chen[1,2], Ran Li[1,2], WeiWei Cao[1,2], Jun Zhu[1,2], YongLin Bai[1,2], Le Wang[3], and Fei He[4*]

[1]Key Laboratory of Ultra-fast Photoelectric Diagnostics Technology, Chinese Academy of Sciences, Xi'an 710119, China;

[2]Institute of Optics and Precisian Mechanics, Xi'an 710119, China;

[3]National Astronomical Observatories, Chinese Academy of Sciences, Beijing 100101, China;

[4]Institute of Geology and Geophysics, Chinese Academy of Sciences, Beijing 100029, China

Key Points:

- A middle and near ultraviolet spectrograph (MN-UVS) was developed to measure the UV radiation background of the upper atmosphere.
- The spectral range of MN-UVS is 200–400 nm with a spectral resolution of better than 2.0 nm.
- The MN-UVS has flown several times on stratospheric balloons and has successfully obtained atmospheric UV spectra at different altitudes.

Citation: Sun, X., Shi, D. L., Chen, Z., Li, R., Cao, W. W., Zhu, J., Bai, Y. L., Wang, L., and He, F. (2023). Middle and near ultraviolet spectrograph of the Scientific Experimental system in Near SpacE (SENSE). *Earth Planet. Phys.*, *7*(6), 655–664. http://doi.org/10.26464/epp2023081

Abstract: The Scientific Experimental system in Near SpacE (SENSE) consists of different types of instruments that will be installed on a balloon-based platform to characterize near-space environmental parameters. As one of the main scientific payloads, the middle and near ultraviolet spectrograph (MN-UVS) will provide full spectra coverage from middle ultraviolet (MUV, 200–300 nm) to near ultraviolet (NUV, 300–400 nm) with a spectral resolution of 2 nm. Its primary mission is to acquire data regarding the UV radiation background of the upper atmosphere. The MN-UVS is made up of six primary components: a fore-optical module, an imaging grating module, a UV intensified focal plane module, a titanium alloy frame, a spectrometer control module, and a data processing module. This paper presents in detail the engineering design of each functional unit of the MN-UVS, as well as the instrument's radiometric calibration, wavelength calibration, impact test, and low-pressure discharge test. Furthermore, we are able to report ground test and flight test results of high quality, showing that the MN-UVS has a promising future in upcoming near-space applications.

Keywords: ultraviolet spectrograph; radiation background; imaging grating; intensified detector; low-pressure discharge; spectral calibration

1. Introduction

The physical processes in near space (altitude 20–100 km approximately) can be very complicated. Accurate observational data are required if our physical models are to be verified and refined (Picone et al., 2002). Recent research shows that the transportation and spatial distribution of ultraviolet (UV) radiation in near space are factors of great importance to our understanding of Earth's spatial environment, especially with regard to its effects on living organisms (Fan DD et al., 2015; Khodadad et al., 2017). However, atmospheric absorption and scattering make it almost impossible to acquire these data by ground-based instruments. Accordingly, most international UV spectrometers or spectral imagers have been spaceborne, but orbital nadir observation mode restricts these devices to UV back scattering radiation only; satellites cannot provide data on UV front scattering and transmission.

The ideal platform for near-space UV detection is the high-altitude balloon (Wang ZC et al., 2020). Balloons can be stable and relatively stationary to the targets, and are therefore suitable for carrying optical instruments that require long integration times to increase their lower detection limits. A high-altitude balloon can reach 35 km or higher, avoiding the major portion of atmospheric absorption of UV radiation. Specifications of some typical international balloon-borne UV instruments (Pommereau, and Piquard, 1994; Renard et al., 1998; Ferlemann et al., 2000; Renard et al., 2000; Pundt et al., 2002; Tuttle et al., 2010) are listed in Table 1.

Supported by the strategic priority research program of the Chinese Academy of Sciences, our primary goal is to build a wide spectral range UV spectrometer, MN-UVS, covering 200 nm to 400 nm，to obtain UV spectra at different zenith angles (using a

Correspondence to: X. Sun, sunxin@opt.ac.cn
F. He, hefei@mail.iggcas.ac.cn
Received 23 MAY 2023; Accepted 20 SEP 2023.
First Published online 12 OCT 2023.

Table 1. UV instrument specifications — selected from representative international balloon-based experiments.

Instrument	Spectral range	Spectral resolution
SAOZ	300–600 nm	0.6 nm
AMON	300–400 nm	0.9 nm
	475–550 nm	0.7 nm
DOAS	320.6–422.6 nm	0.45 nm (UV)
	417.6–670.7 nm	1.48 nm (VIS)
SAOZ-BrO	320–400 nm	0.9 nm
SALOMON	350–700 nm	0.34 nm
FIREBall	190–225 nm	0.04 nm

turntable) on a high-altitude balloon platform (altitude no less than 25 km).

Scientific and engineering goals of the MN-UVS are: (1) to obtain spectrograms ranging from MUV to NUV of the near-space atmosphere background, and to establish a Chinese near-space UV background database; (2) to provide reference data that will allow removal of background from data collected by planetary remote sensing devices or instruments; (3) to provide reference UV radiation data for biological study, by flight with bio-exposure devices; (4) to test the environmental adaptability of high-voltage devices in the complicated low-pressure environment of near-space.

2. Function and Performance

The main functional requirements of MN-UVS are listed as: (1) able to acquire valid spectral data of MUV and NUV during daytime while the balloon reaches cruise altitude; (2) capable of automatic thermal control of the optomechanical system; (3) be operational during ascent and descent; (4) able to monitor spectral curve variation in quasi real-time in the ground command center; (5) capable of automatic control of exposure time and gain; manual backup control will take over when the automatic mode fails.

The main technical specifications of MN-UVS are shown in Table 2.The optomechanical part of MN-UVS is designed to be a sealed capsule with ability to maintain 0.5 air pressure difference. Specially designed valves allow the inner chamber to be inflated with pure nitrogen before flight to protect the optical parts. The design provides protection for the intensified detector module as well.

Table 2. Technical performance requirements of MN-UVS.

Parameter	Values
Working spectral range	200–400 nm
Spectral resolution	≤ 2 nm
Field of view	1° × 0.04°
Counting rate	2 counts/s/pixel/R
Integration time	1–10 s
Radiometric calibration	≤ 15%
Weight	30 kg
Power consumption	≤ 96 W (average)
	≤ 200 W (peak)
Data rate	≤ 54 k bps

3. Instrument Design

3.1 Theory

Generally, two basic types of spectrographs are used to acquire spatial and spectral information directly from a target; they employ different detectors and scanning mechanisms. As illustrated in Figure 1 (left), one uses a linear array detector; at each exposure, the detector records spectral information from a single object point. Therefore, to cover an extended target area, the system needs a swing-mirror unit to perform a "whiskbroom" motion along the scanning direction. This method takes an enormous amount of time to cover the desired object space; coverage gaps are inevitable. The other approach, Figure 1 (right), uses a focal plane array (FPA); it can record both spatial and spectral data from multiple adjacent object points. By push-broom alone in the moving direction, this approach obtains full coverage of spatial and spectral information from a two-dimensional object.

It is apparent that the push-broom setup is more suitable for the remote sensing that SENSE is designed to perform. The slit size of the UV spectrograph is adjustable according to different sampling areas and desired levels of spectral accuracy; under some circumstances — for example, when spatial resolution is less important — it can be advantageous to accumulate weak signals along the spatial dimension. In this mission, the targets are small volumes of atmosphere, each of which can be treated as a uniform mass, ignoring its internal spatial differences. This means we can use the average value of the spectral response along the spatial dimension to reduce random noise caused by the detector array.

In Figure 2, X_i stands for pixels spatially distributed along the slit, which are reimaged on the detector plane in the same sequence; λ_i stands for the central wavelength of each equal wavelength

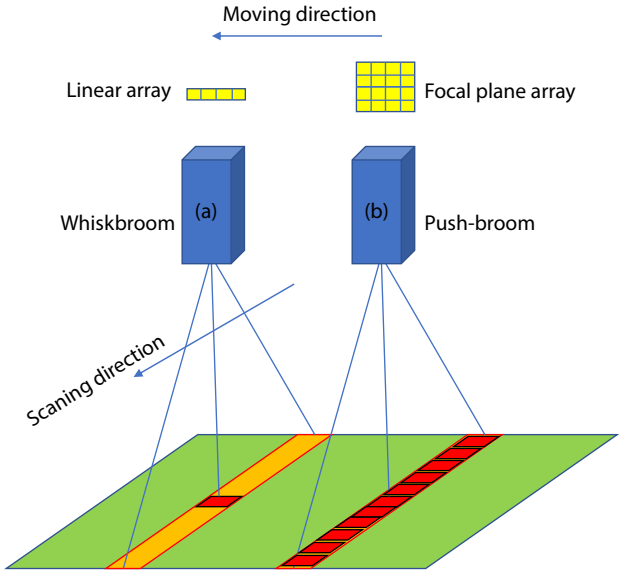

Figure 1. Schematic diagram of (a) whiskbroom and (b) push-broom spectrograph scanning.

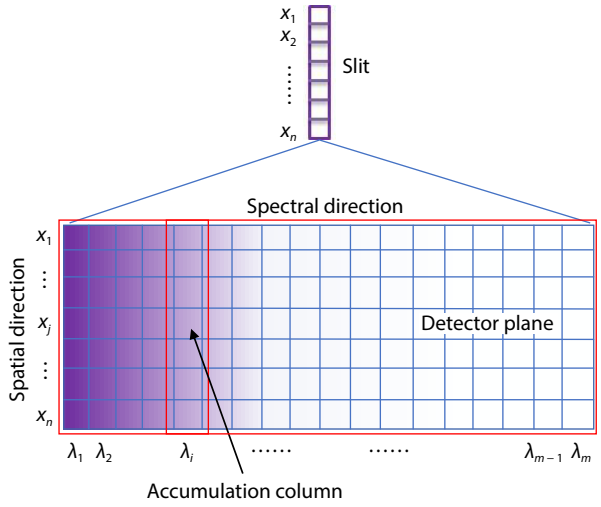

Figure 2. Schematic diagram: Method of reducing random noise by accumulating detailed spectral data along a spatial interval.

interval of the target spectrum, consistent with the dispersion direction of the grating. By data accumulation in each column, the readout intensity at each different spatial unit is added up for each spectral interval λ_i. Since the total readout noise is also accumulated, and since it is the square root of the quadratic sum of noise produced by each line, the signal-to-noise ratio (SNR) of the spectrum is improved by column accumulation of each λ_i:

$$\mathrm{SNR}_A = \frac{S_A}{N_A} = \frac{\sum_{j=1\sim n} S_j}{\sqrt{\sum_{j=1\sim n} N_j^2}} = \frac{nS_o}{\sqrt{n}N_o} = \sqrt{n}\frac{S_o}{N_o} > \frac{S_o}{N_o},$$

where S_A is the accumulated signal intensity along the spatial direction, N_A is the accumulated noise, and n stands for the number of spatial units (pixels). We assume that the original spectral signals of each spatial line are approximately equal and can be indicated by S_o; we make a similar assumption about the equality of the original readout noise of each line, indicated by N_o. From the equation one can tell that column accumulation yields a final SNR of the spectrum that is improved by a factor of $\sqrt{n}$.

3.2 System Composition

The MUV-NUV spectrograph is designed to fly via high-altitude balloon at around 25–35 km height. Considering the lift force limitation that applies to almost all balloon platforms, the requirement of lightweight and compact design is inevitable. The MUV-NUV spectrograph includes two individual modules: a spectrograph module and a control module. The two parts are connected by cables with a LEMO interface. The spectrograph module includes a reflective mirror, an imaging grating, and an intensified charge coupled device (ICCD) module. The small chamber in the optomechanical frame carries additional modules: a gating module and a power supply module that provides 200 volts for gating and 6000 volts for gain adjustment of the intensifier.

3.3 System Design

3.3.1 Optical system design

The primary task of this mission is to measure accurately the background UV spectrum of the high-altitude atmosphere. Due to the relatively high uniformity of the atmosphere at that level, it is not mandatory for the spectrographic investigation to determine the spatial distribution of the UV spectrum at that altitude. This allows great flexibility to improve the spectral resolution and sensitivity of the spectrograph, goals that are crucial to the success of the mission.

The two suitable optical setups for data collection in the UV band are called the Czerny-Turner (CT) setup and the Wadsworth setup. The CT setup is regarded as the most adaptable structure for UV to FUV (far ultraviolet) band remote sensing devices; many satellite-based instruments have been of this sort (Austin et al., 2009). Taking the Ionospheric Connection Explorer (ICON) for example (Mende et al., 2017), the FUV imager achieved 4 nm spectral resolution in two FUV bands with angular resolution of 0.1 degree (Loicq et al., 2016; Frey et al., 2023). Such high performance of the CT setup is credited to its complex composition, which involves at least four optical elements (see Figure 3). The Wadsworth setup is also widely used in the UV spectral imaging (Bartoe and Brueckner, 1975; Howle et al., 2005; Kimura et al., 2010); however, it uses a curved grating to realize both dispersion and refocusing. One can take it as a relay-lens used in a situation of finite conjugation. The result is that the collimating and imaging reflectors are reduced to a single so-called "imaging grating", making adjustment of the Wadsworth much easier.

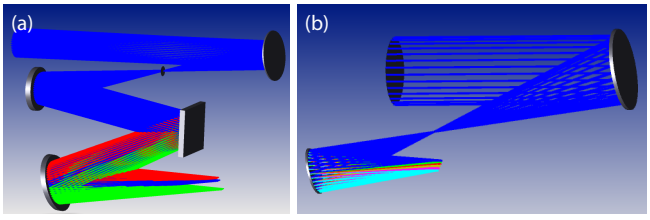

Figure 3. (a) CT setup schematic; (b) Wadsworth setup schematic.

The goals and platform of this mission strongly suggested that the Wadsworth setup would be our best choice. Nevertheless, based on instrument payload restrictions, specifically, the volume, working spectrum range, and overall diffraction efficiency, we studied a series of commercial products and chose a Horiba No.52301020 spherical imaging grating. The grating has a flat image plane over a large range of its working spectrum (190–455.6 nm) thanks to its variable line spacing groove feature. It also has moderate installation restraints, which give flexibility to the forthcoming system alignment.

A simulation of the performance of the Horiba grating is presented in Figure 4. The width of the input slit is set to 60 μm and 70 μm for comparison. The simulation results reveal several crucial features that help us to estimate the final imaging status at the image plane. The spots diagram and the cross-section profiles together give the trend of energy concentration along each successive wavelength increment. The most important performance marker is the bandpass (FWHM, full width at half maximum) of each calculated center wavelength; these are listed in the columns on the right. Note that when the input slit is 60 μm,

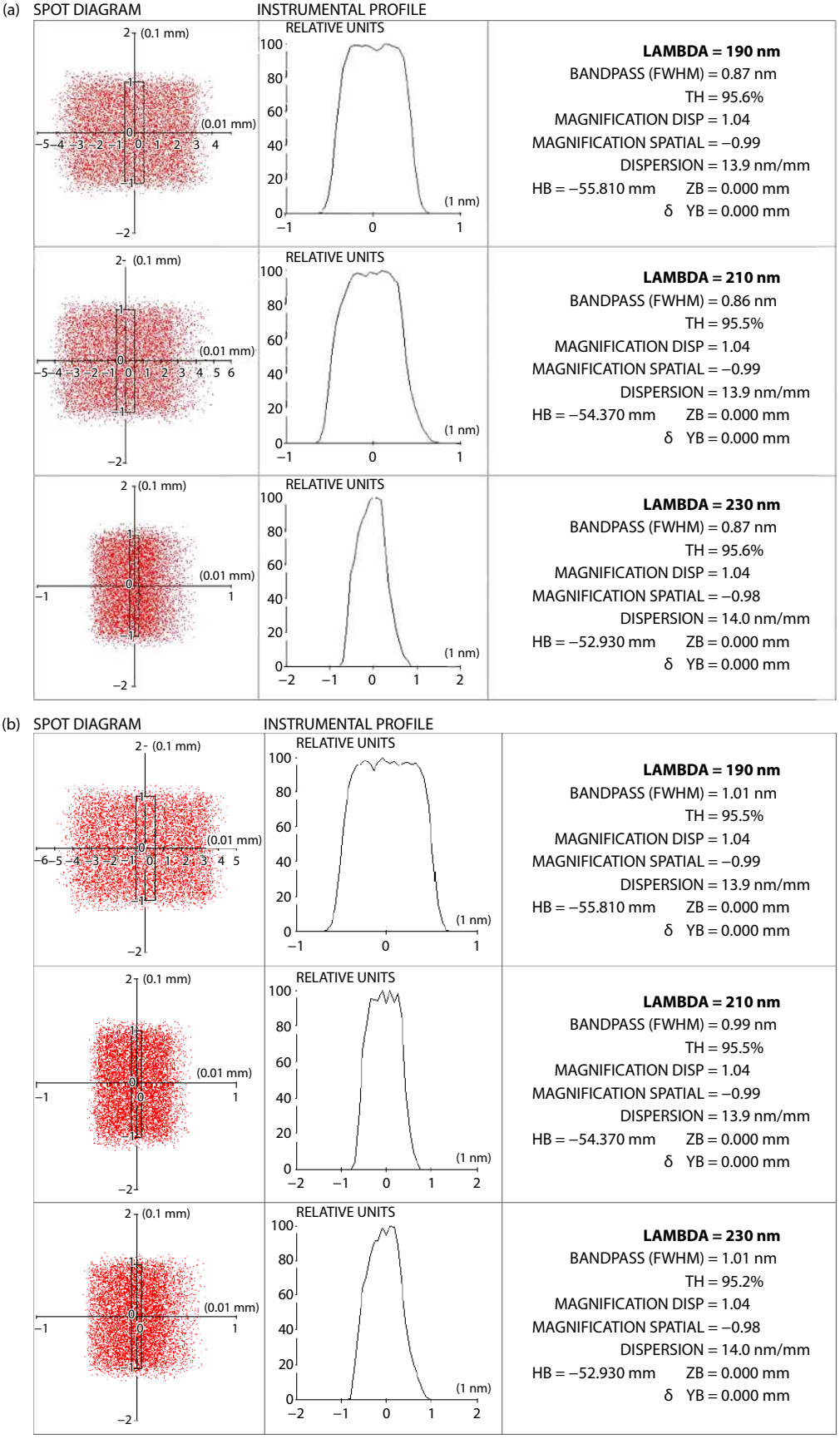

Figure 4. Simulated performance of the Horiba No.52301020 spherical imaging grating. (a) Spot diagram and instrumental profile at 60 μm slit width; (b) Spot diagram and instrumental profile at 70 μm slit width.

the FWHM of each chosen wavelength is more stable than when the slit size is 70 μm.

Since the grating simultaneously realizes dispersion and imaging, and the simulated performance delivers a satisfactory result, we use a decentered paraboloid reflector as the telescope to collect radiation from the target. The reflector gives an intermediate image of the target at the slit position; it will then be dispersed and re-imaged at the detector plane, as shown in Figure 5, below. The field of view of the MN-UVS is 1° × 0.04°, within which the atmospheric radiation can be regarded as from a uniform source; therefore, data in the spatial dimension can be added together to increase the SNR of the MN-UVS.

3.3.2 Intensified detector design and assembly

The detector used in MN-UVS is an intensified complementary metal oxide semiconductor (ICMOS) detector; it consists of an image intensifier and a CMOS chip. This detector was designed for dynamic UV spectrum analysis, especially for radiation from a weak target source. The intensifier receives the UV radiation incoming from the target and turns this radiation into photoelectrons using a piece of photocathode with high quantum efficiency, as shown in Figure 6. The photoelectrons are multiplied by micro channel plate (MCP) A and projected to the fluorescent screen, where they generate photons in the visible spectrum. MCP B delivers the output photons to the sensor plane of the CMOS chip. Both the image intensifier and the CMOS chip are UV band-enhanced to minimize the lower threshold of the intensified detector unit.

The gating voltage acts as a switch of the detector unit, controlling the 'on' and 'off' of the incoming radiation. Its voltage alternates between +50 and −200 V, determining whether the input photons pass through or are rejected.

The image intensifier is a Hi-QE Blue (high quantum efficiency in UV band) shelf product with a diameter of 18 mm provided by Photonic Inc. (Figure 7). It is coupled to a commercial CMOS camera, Imperx 2020, with a piece of thin MCP. The protective window of the CMOS chip is removed to meet the coupling requirement. The coupling test system is composed of a collimator (F# = 10, focal length = 500 mm) with a lithography resolution chart (USAF1951 standard). The resolution chart is separated from the collimator's focal plane to create a 1: 1 image on the front of

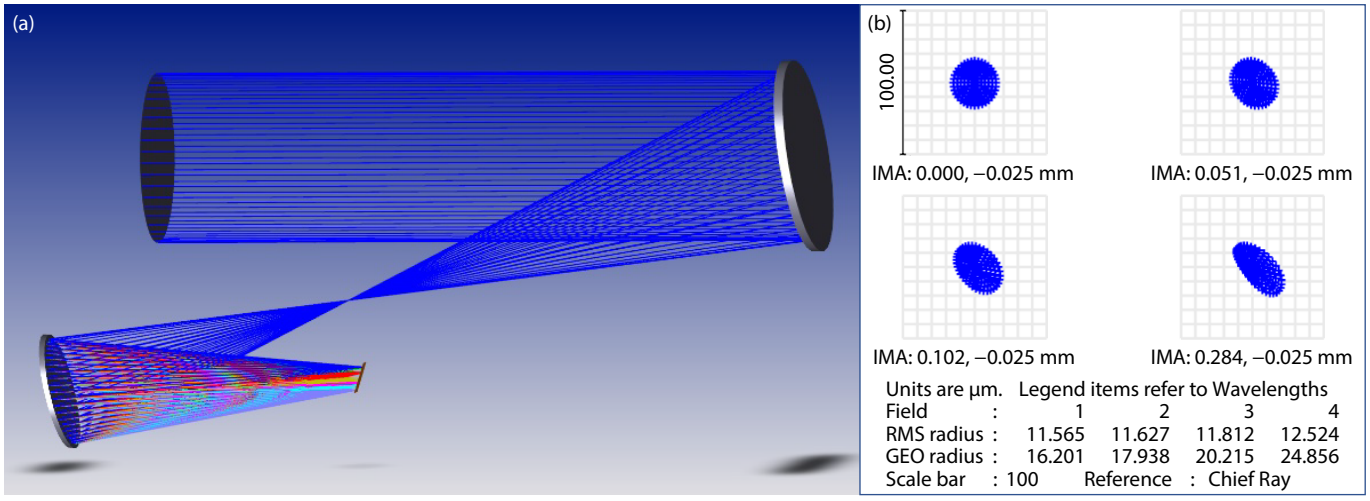

Figure 5. (a) Optical schematic of MN-UVS; (b) Spot diagram at the intermediate image plane.

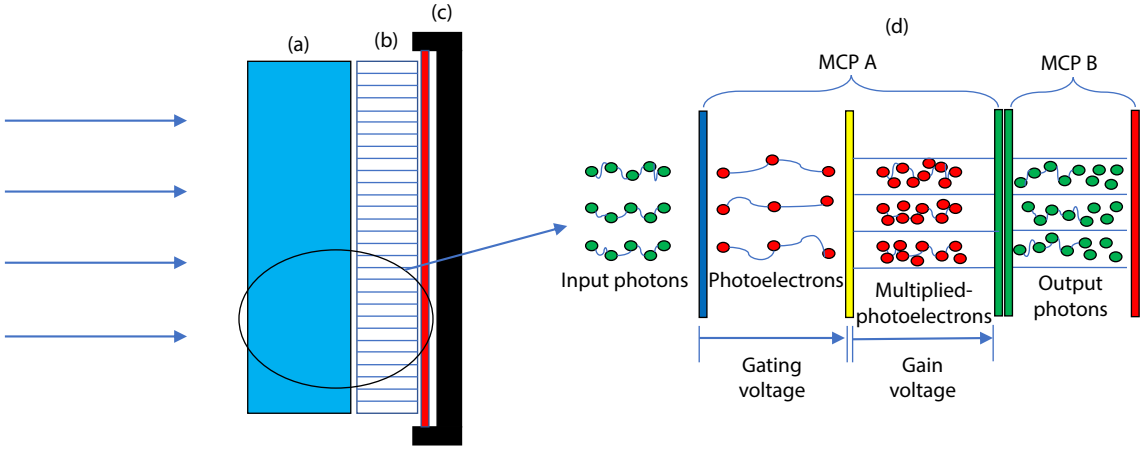

Figure 6. Schematic of the intensified detector. (a) MCP A with photocathode on the front surface; (b) MCP B as the output window of the intensifier; (c) CMOS chip with its protective window removed; (d) illustration of the photoelectron multiplier process.

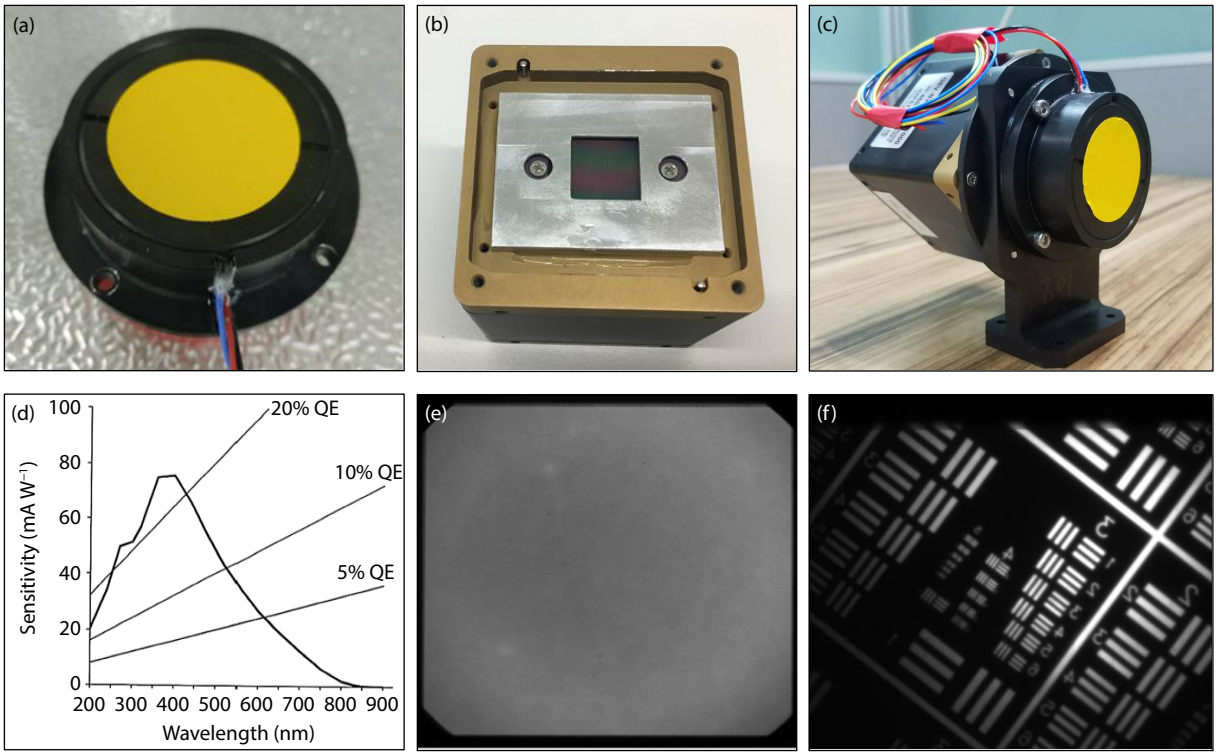

Figure 7. (a) The image intensifier unit; (b) Imperx 2020 with protective window removed; (c) The coupled image intensified-CMOS unit; (d) The QE of the image intensifier; (e) The uniformity test of the image intensified-CMOS unit; (f) The resolution test of the image intensified-CMOS unit.

the photocathode; thus the image quality is the indicator of whether the ICMOS is adjusted to the best position. Testing results show that the ICMOS unit achieves spatial resolution of 25 lp/mm.

4. Instrument Calibration

The spectral calibration of the MN-UVS includes three key steps: testing of spectral range, spectral resolution, and spectral accuracy. The calibration setup is shown in Figure 8. A low-pressure mercury lamp (LPML) is used to illuminate a slit (1 mm × 4 mm) at the focal plane of a customized UV-collimator. The collimated UV radiation enters the MN-UVS and is reimaged in the form of wavelength-specific strips at the detector plane.

The LPML has several stable atomic emission lines within the spectral range of 250 nm to 420 nm. According to the National Institute of Standards and Technology (NIST) standard, the wavelength accuracy of these atomic emission lines are ±0.0001 nm, and the spectral width is approximately 0.00025 nm. Therefore, the LPML is regarded as an ideal reference source for the MN-UVS's spectral calibration.

To complete the spectral calibration, the main task is to generate the wavelength calibration function as follows:

$$\lambda_x = ax + \lambda_0,$$

where λ_x is wavelength at x pixel, a is the calibration coefficient, and λ_0 is the wavelength at the first pixel, where $x = 0$; x is the pixel position on the detector plane; a and λ_0 are acquired by linear fitting of the LPML spectrum data taken by the MN-UVS,

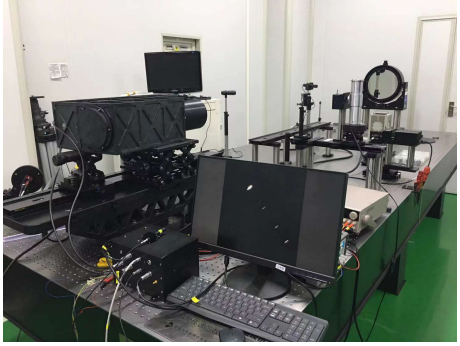

Figure 8. The calibration setup for MN-UVS.

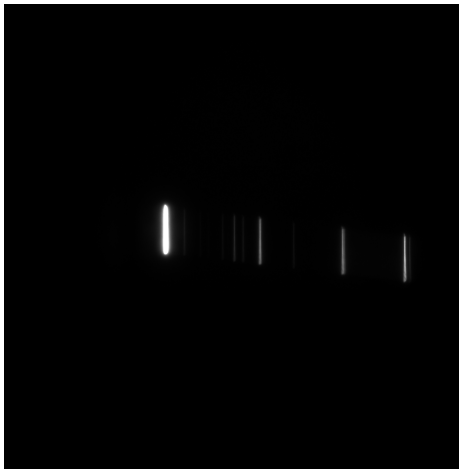

Figure 9. LPML spectrum image taken by the MN-UVS.

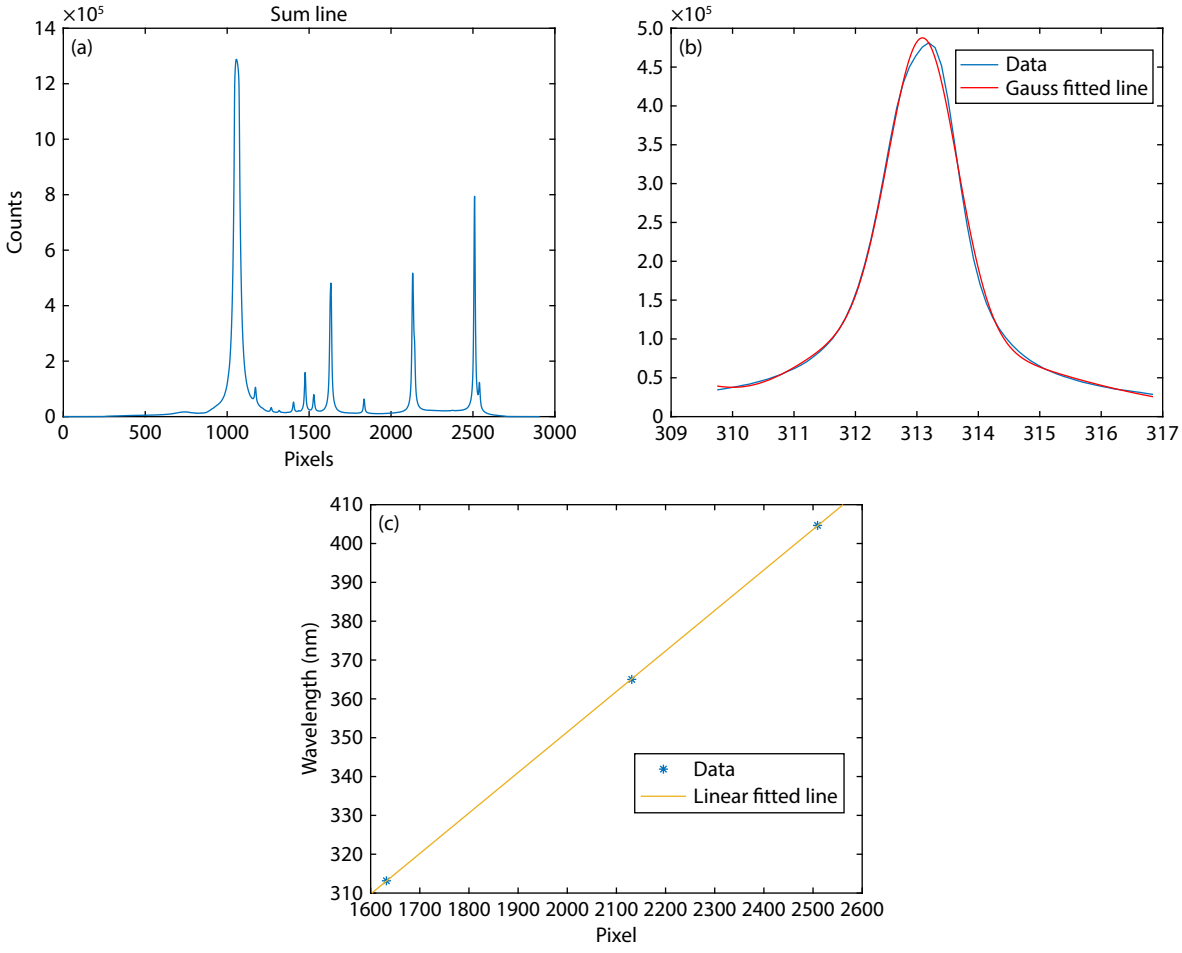

Figure 10. (a) LPML spectrum data taken by the MN-UVS; (b) Gauss fitting to find the LPML spectrum peaks; (c) Linear fitting of the peaks and their pixel coordinates.

since the MN-UVS's grate intervals are assumed to be linear.

First, the gain level and integrated time of the detector unit are adjusted to result in a stable, non-saturated image (see Figure 9).
Second, the image data are processed into a spectrum chart, shown in Figure 10a, according to the location of 253.65 nm (the strongest characteristic peak of the LPML); the three other sharp peaks are identified and compared to their LPML reference wavelengths (313.16 nm, 365.01 nm, and 404.66 nm).
Third, the peak wavelengths and the corresponding pixel coordinates are linear fitted to calculate a (0.1023) and λ_0 (152.4 nm). The fitting quality result is shown in Figure 10c. The determined coefficient is $r^2 = 1$ and the standard error is 0.0827, indicating a good fit.
Finally, the instrument's spectral range is obtained by putting pixel position x into the calibration function to obtain λ_{start} = 189.78 nm and λ_{end} = 418.21 nm, where λ_{start} is the wavelength at position X_{start}, and λ_{end} is the wavelength at position X_{end}. X_{start} and X_{end} are determined according to the target limits of MN-UVS's spectral range, which are 200 nm to 400 nm.

The wavelength calibration function can now be used to generate a spectrum chart of the LPLM, in the form of photon counts versus calibrated wavelength, as shown in Figure 11.

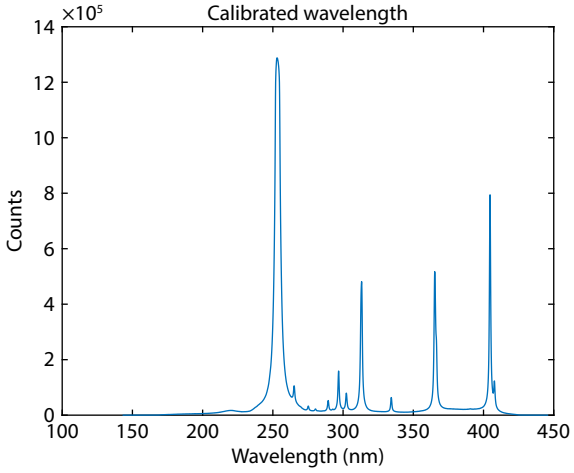

Figure 11. LPML spectrum taken by MN-UVS after wavelength calibration.

Four known and independent LPML spectral lines were chosen to test the spectral resolution of the instrument. The profile of each detected line is Gaussian-fitted to determine its peak and FWHM value. The spectral resolution is the average FWHM value of each peak. The results are shown in the Table 3. The spectral accuracy is

Table 3. FWHM results of four characteristic wavelengths.

Characteristic wavelength (nm)	FWHM (nm)
313.65	1.43
365.01	2.01
404.66	1.31
Average value	1.58

Table 4. Differences between tested characteristic wavelengths and NIST standards.

LPML characteristic wavelengths of the NIST standard (nm)	Peaks of the MN-UVS LPML spectrum (nm)	Errors (nm)
253.65	253.33	−0.32
302.15	302.5	+0.35
334.15	334.3	+0.15
Average error		0.27

calculated by comparing the peaks in the generated LPML spectrum in Table 4 with the LPML characteristic wavelengths according to the NIST standard. The spectral accuracy of the instrument is the average value of the errors, which is 0.27 nm for the NM-UVS.

The radiometric calibration setup of the MN-UVS is shown in Figure 12. The UV enhanced radiant source is a laser bumped lamp with spectral irradiance calibrated in Physikalisch-Technische Bundesanstalt (PTB). The diffuser is illuminated in the nominal direction by the UV source. The reflection of the diffuser on the angle of 45° to the nominal of the diffuser has also been calibrated. The MN-UVS is placed at a side with an angle of 45° to the nominal angle of the diffuser. The UV radiation reflected by the diffuser enters the MN-UVS and is then dispersed and reimaged at the detector plane.

The output image is then processed to a spectral line. The absolute calibration coefficient is calculated according to the spectral irradiance reflected by the diffuser; the output spectral line of the MN-UVS, shown in Figure 13.

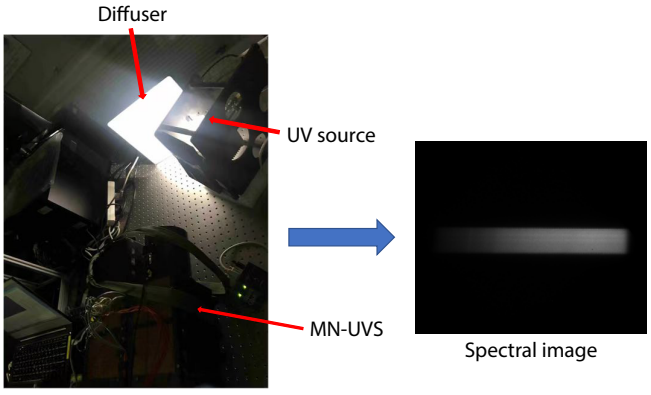

Figure 12. The radiometric calibration setup and image output of the MN-UVS.

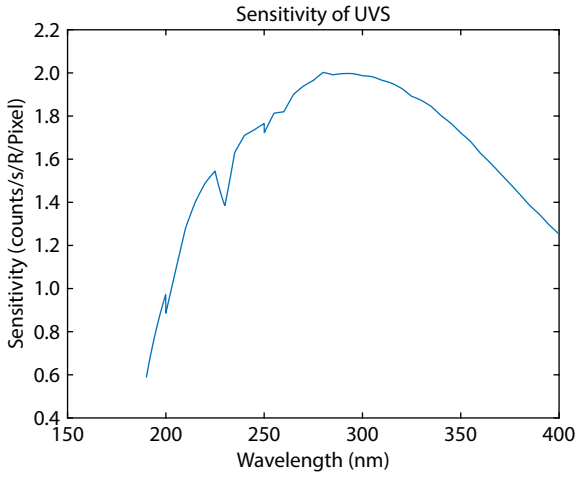

Figure 13. Calibration coefficients of the MN-UVS.

The absolute radiometric calibration uncertainty of the MN-UVS is calculated according to the calibration method. The results are

Table 5. Uncertainties of the MN-UVS absolute radiometric calibration.

Parameters	Uncertainties				
	λ = 200 nm	λ = 250 nm	λ = 300 nm	λ = 350 nm	λ = 400 nm
Temporal stability of the UV source	0.1%	0.1%	0.1%	0.1%	0.1%
Irradiance uncertainty of the UV light source	5.50%	2.04%	1.87%	1.86%	1.77%
Non-uniform of the UV source	1.15%	1.15%	1.15%	1.15%	1.15%
Reflectivity uncertainty of the diffuser	0.50%	0.50%	0.50%	0.50%	0.50%
Uncertainty of the distance	0.58%	0.58%	0.58%	0.58%	0.58%
Non-uniform of the MN-UVS	0.50%	0.50%	0.50%	0.50%	0.50%
Nonlinearity of the detector	0.58%	0.58%	0.58%	0.58%	0.58%
Uncertainty of the gain of the ICCD	1.5%	1.5%	1.5%	1.5%	1.5%
Noise	1.15%	1.15%	1.15%	1.15%	1.15%
Uncertainty of the spectral calibration	0.15%	0.12%	0.10%	0.08%	0.07%
Overall extended uncertainty (k=2)	12.0%	6.4%	6.2%	6.1%	6.0%
Overall standard uncertainty (k=1)	6.0%	3.2%	3.1%	3.1%	3.0%

shown in Table 5. The worst of the extended uncertainty (k = 2) is 12% at a wavelength of 200 nm, and the best is roughly 6% at wavelengths ranging from 250 nm to 400 nm. The worst of the standard uncertainty (k = 1) is 6% at 200 nm, and the best is roughly 3% at wavelengths from 250 nm to 400 nm. The extended uncertainty (k = 2) meets the 15% target demand of the system in the range from 200 nm to 400 nm.

5. Preliminary Results

After laboratory tests, the MN-UVS was tested on the ground and on the balloon platform. The experiments were conducted at Da Qaidam on the Tibetan Plateau. Figure 14 shows the atmospheric background UV spectra obtained on the ground and on the balloon platform during the HH-20-9 experiment of SENSE in August 2020. Both spectra were measured at a local zenith angle of 60°. The HH-20-9 experiment was combined with a near-space biological exposure experiment (Lin W et al., 2022, Liu J et al., 2022). This is the first time a biological exposure experiment was equipped with a MN-UVS. Due to its absorption by atmospheric ozone, UV radiation at wavelengths shorter than 280 nm cannot reach the ground at 3 km elevation above sea level (ASL). At an altitude of 32 km ASL, UV radiation is significantly increased. The ozone absorption edge around 300 nm is still clear. An interesting feature is the significant increase of radiation at wavelengths shorter than 220 nm, mainly due to reduced ozone absorption since the observation altitude is well above the peak ozone altitude, which is approximately 20 km.

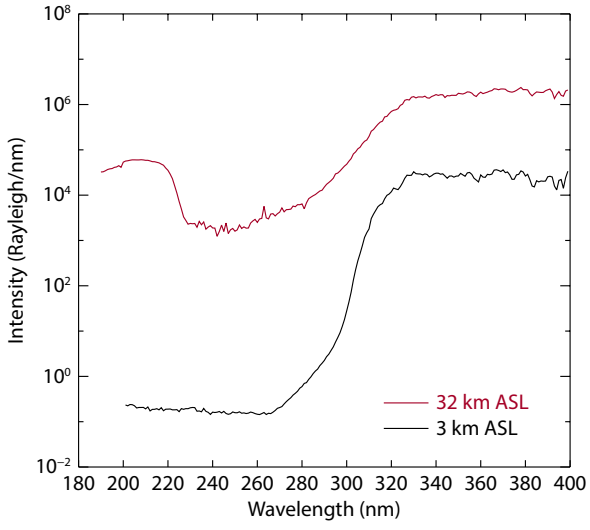

Figure 14. UV spectra obtained by the MN-UVS on the ground (black) and on the balloon platform at 32 km above sea level (ASL, red).

6. Summary

The MN-UVS is one of the main payloads of the SENSE. This paper presents details of the MN-UVS system design, its detector design, and its calibration test results. From 2020 to 2022, the MN-UVS was deployed in several balloon-based experiments, especially with biological exposure instruments. The UV spectra obtained by the MN-UVS will provide important information for near-space astrobiology research and in studies of radiation transportation in Earth's atmosphere (e.g., Zhang JQ et al., 2019; Shen JX et al., 2022) and can potentially be applied to the near space of other planets (Wei Y et al., 2017). More balloon-based experiments will be conducted in the future to characterize in detail the properties of background UV radiation at different regions, different altitudes, and different solar zenith angles.

Acknowledgments

This work was supported by the Strategic Priority Research Program of the Chinese Academy of Sciences (grant XDA17010203, XDA17010201).

References

Austin, D. R., Witting, T., and Walmsley, I. A. (2009). Broadband astigmatism-free Czerny-Turner imaging spectrometer using spherical mirrors. *Appl. Opt.*, *48*(19), 3846–3853. https://doi.org/10.1364/AO.48.003846

Bartoe, J. D. F., and Brueckner, G. E. (1975). New stigmatic, coma-free, concave-grating spectrograph. *J. Opt. Soc. Am.*, *65*(1), 13–21. https://doi.org/10.1364/JOSA.65.000013

Fan, D. D., Chen, X. F., Li, Z. Q., and Mei, X. D. (2015). Radiation environment study of near space in China Area. In *Proceedings Volume 9640, Remote Sensing of Clouds and the Atmosphere XX* (pp. 231-235). Toulouse, France: SPIE. https://doi.org/10.1117/12.2194050

Ferlemann, F., Bauer, N., Fitzenberger, R., Harder, H., Osterkamp, H., Perner, D., Platt, U., Schneider, M., Vradelis, P., and Pfeilsticker, K. (2000). Differential optical absorption spectroscopy instrument for stratospheric balloonborne trace-gas studies. *Appl. Opt.*, *39*(15), 2377–2386. https://doi.org/10.1364/AO.39.002377

Frey, H. U., Mende, S. B., Meier, R. R., Kamaci, U., Urco, J. M., Kamalabadi, F., England, S. L., and Immel, T. J. (2023). In flight performance of the far ultraviolet instrument (FUV) on ICON. *Space Sci. Rev.*, *219*(3), 23. https://doi.org/10.1007/S11214-023-00969-9

Howle, C. R., Ali, S., Tuckett, R. P., Shaw, D. A., and West, J. B. (2005). Characterisation of a new VUV beamline at the Daresbury SRS using a dispersed fluorescence apparatus incorporating CCD detection. *Nucl. Instrum. Methods Phys. Res. B*, *237*(3-4), 656–665. https://doi.org/10.1016/j.nimb.2005.03.287

Khodadad, C. L., Wong, G. M., James, L. M., Thakrar, P. J., Lane, M. A., Catechis, J. A., and Smith, D. J. (2017). Stratosphere conditions inactivate bacterial endospores from a mars spacecraft assembly facility. *Astrobiology*, *17*(4), 337–350. https://doi.org/10.1089/ast.2016.1549

Kimura, S. I., Ito, T., Sakai, M., Nakamura, E., Kondo, N., Horigome, T., Hayashi, K., Hosaka, M., Katoh, M., … Soda, K. (2010). SAMRAI: A novel variably polarized angle-resolved photoemission beamline in the VUV region at UVSOR-II. *Rev. Sci. Instrum.*, *81*(5), 053104. https://doi.org/10.1063/1.3425778

Lin, W., He, F., Zhang, W. S., Yao, Z. H., Shen, J. X., Ren, Z. P., Yuan, H., Cai, R., Wei, Y., and Pan, Y. X. (2022). Astrobiology at altitude in Earth's near space. *Nat. Astron.*, *6*(2), 289–289. https://doi.org/10.1038/s41550-022-01606-1

Liu, J., Zhang, W. S., He, K., Liu, L., Wang, C., Jiang, Y. D., Ma, S. J., Tian, J. S., Li, Y., … Lin, W. (2022). Survival of the magnetotactic bacterium *Magnetospirillum gryphiswaldense* exposed to Earth's lower near space. *Sci. Bull.*, *67*(13), 1335–1339. https://doi.org/10.1016/j.scib.2022.03.005

Loicq, J., Kintziger, C., Mazzoli, A., Miller, T., Chou, C., Frey, H. U., Immel, T. J., and Mende, S. B. (2016). Optical design and optical properties of a VUV spectrographic imager for ICON mission. In *Proceedings Volume 9905, Space Telescopes and Instrumentation 2016: Ultraviolet to Gamma Ray* (pp. 54-69). Edinburgh, United Kingdom: SPIE. https://doi.org/10.1117/12.2232588

Mende, S. B., Frey, H. U., Rider, K., Chou, C., Harris, S. E., Siegmund, O. H. W., England, S. L., Wilkins, C., Craig, W., … Ellis, S. (2017). The far ultra-violet imager on the icon mission. *Space Sci. Rev.*, *212*(1-2), 655–696. https://doi.org/10.1007/s11214-017-0386-0

Picone, J. M., Hedin, A. E., Drob, D. P., and Aikin, A. C. (2002). NRLMSISE-00

empirical model of the atmosphere: Statistical comparisons and scientific issues. *J. Geophys. Res.: Space Phys.*, *107*(A12), 1468. https://doi.org/10.1029/2002JA009430

Pommereau, J. P., and Piquard, J. (1994). Ozone and nitrogen dioxide vertical distributions by UV-visible solar occultation from balloons. *Geophys. Res. Lett.*, *21*(13), 1227–1230. https://doi.org/10.1029/94GL00389

Pundt, I., Pommereau, J. P., Chipperfield, M. P., Van Roozendael, M., and Goutail, F. (2002). Climatology of the stratospheric BrO vertical distribution by balloon-borne UV-visible spectrometry. *J. Geophys. Res.: Atmos.*, *107*(D24), 4806. https://doi.org/10.1029/2002JD002230

Renard, J. B., Pirre, M., Robert, C., and Huguenin, D. (1998). The possible detection of OBrO in the stratosphere. *J. Geophys. Res.: Atmos.*, *103*(D19), 25383–25395. https://doi.org/10.1029/98JD01805

Renard, J. B., Chartier, M., Robert, C., Chalumeau, G., Berthet, G., Pirre, M., Pommereau, J. P., and Goutail, F. (2000). SALOMON: a new, light balloonborne UV-visible spectrometer for nighttime observations of stratospheric trace-gas species. *Appl. Opt.*, *39*(3), 386–392. https://doi.org/10.1364/AO.39.000386

Shen, J. X., Chen, Y., Sun, Y., Liu, L., Pan, Y. X., and Lin, W. (2022). Detection of biosignatures in Terrestrial analogs of Martian regions: Strategical and technical assessments. *Earth Planet. Phys.*, *6*(5), 431–450 https://doi.org/10.26464/epp2022042

Tuttle, S. E., Schiminovich, D., Grange, R., Rahman, S., Matuszewski, M., Milliard, B., Deharveng, J. M., and Martin, D. C. (2010). FIREBALL: The first ultraviolet fiber fed spectrograph. In *Proceedings Volume 7732, Space Telescopes and Instrumentation 2010 - Ultraviolet to Gamma Ray* (pp. 718-732). San Diego, CA, United States: SPIE. https://doi.org/10.1117/12.857877

Wang, Z. C., Huang, M., Qian, L. L., Zhao, B. W., and Wang, G. M. (2020). High-altitude balloon-based sensor system design and implementation. *Sensors*, *20*(7), 2080. https://doi.org/10.3390/s20072080

Wei, Y., Yue, X. A., Rong, Z. J., Pan, Y. X., Wan, W. X., and Zhu, R. X. (2017). A planetary perspective on Earth's space environment evolution. *Earth Planet. Phys.*, *1*(1), 63–67 https://doi.org/10.26464/epp2017009

Zhang, J. Q., Liu, Y., Chen, H. B., Cai, Z. N., Bai, Z. X., Ran, L. K., Luo, T., Yang, J., Wang, Y. N., … Lu, D. R. (2019). A multi-location joint field observation of the stratosphere and troposphere over the Tibetan Plateau. *Earth Planet. Phys.*, *3*(2), 87–92. https://doi.org/10.26464/epp2019017